

Simulation of the Observed Coronal Kink Instability and Its Implications for the SDO/AIA

A.K. Srivastava^a, G.J.J. Botha^b, T.D. Arber^b, P. Kayshap^a

^a*Aryabhata Research Institute of Observational Sciences (ARIES), Manora Peak,
Nainital-263 129, India.*

^b*Physics Department, Centre for Fusion, Space and Astrophysics, University of Warwick,
Coventry CV4 7AL, UK.*

Abstract

Srivastava et al. (2010) have observed a highly twisted coronal loop, which was anchored in AR10960 during the period 04:43 UT-04:52 UT on 4 June 2007. The loop length and radius are approximately 80 Mm and 4 Mm, with a twist of 11.5π . These observations are used as initial conditions in a three dimensional nonlinear magnetohydrodynamic simulation with parallel thermal conduction included. The initial unstable equilibrium evolves into the kink instability, from which synthetic observables are generated for various high-temperature filters of SDO/AIA. These observables include temporal and spatial averaging to account for the resolution and exposure times of SDO/AIA images. Using the simulation results, we describe the implications of coronal kink instability as observables in SDO/AIA filters.

Keywords: magnetohydrodynamics (MHD), magnetic reconnection, corona

Email address: aks@aries.res.in (A.K. Srivastava^a, G.J.J. Botha^b, T.D. Arber^b, P. Kayshap^a)

1. Introduction

The active region magnetic field exhibits complex topology **due to the emergence of new large-scale magnetic flux** from the sub-photospheric layers of the Sun. Such complexity some times generates various types of magnetic instabilities that are well observed in the solar active regions as a trigger of flares and associated dynamical processes (Srivastava et al., 2010; Kumar et al., 2010; Foullon et al., 2011; Innes et al., 2012). Among the various types of magnetic instabilities, the kink instability is most commonly observed in the solar atmosphere, and evolved in the large-scale magnetic flux-tubes due to their azimuthal twist. However, the twist must cross the minimum threshold value of $\Phi > 2.5\pi$ to trigger the kink instability in the magnetic flux-tubes in the solar corona (Hood & Priest, 1979). The kink instability is well observed in active region loops (Srivastava et al., 2010), eruptive filaments (Liu et al., 2008), eruptive coronal cavities (Liu et al., 2007), and it can eventually trigger flares and CMEs (Kliem & Török, 2006; Cho et al., 2009). Recently, Zaqarashvili et al. (2010) have given an important conclusion that the axial mass flow in the magnetic flux-tubes reduces the threshold of kink instability, and can easily lead to solar flares and CMEs. The kink instability does not only liberate the flare energy, it can also cause the excitation of MHD wave modes (Haynes et al., 2008). The kink instabilities observed in the astrophysical plasma are also firstly reproduced in the laboratory experiment (Moser & Bellan, 2012), which shows the confinement of kink unstable twisted plasma structures due to multi-stage cascade reconnection at the laboratory scales.

In addition to the observations the coronal kink instability is studied using analytical and numerical modelling (Mikić et al., 1990; Baty & Heyvaerts, 1996; Arber et al., 1999; Gerrard et al., 2002). The ideal MHD kink instability has been inferred as a trigger for reconnection in the flaring loops (Browning et al., 2008; Hood et al., 2009). Botha et al. (2011) initialised the kink instability with a twisted magnetic field and reported that the inclusion of thermal conduction along magnetic field lines can reduce the maximum reconnection generated temperature by an order of magnitude. This changes the range of spectral lines as observables of the kink instability when compared to simulations without conduction. Botha et al. (2012) have also reported the observational signatures of the MHD kink instability with the inclusion of thermal conduction. A kink-unstable cylindrical loop is evolved by using the initial conditions of a highly twisted loop as observed by TRACE (Srivastava et al., 2010). The numerical results are synthesized through TRACE temperature response function filtering, and through spatial and temporal averaged line of sight intensity measurements (Haynes & Arber, 2007).

In the present paper, we extend the work of Botha et al. (2012) and study the evolution of the kink unstable loop as observed by Srivastava et al. (2010) in the high-temperature filters of SDO/AIA. In Sec. 2 we present a brief description of the numerical model and initial conditions. In Sec. 3 we describe the results related to the synthesis of a kink unstable loop in various SDO/AIA channels. The discussion and conclusions form the last section.

2. Numerical Simulation of the Observed Coronal Kink Instability

The nonlinear three-dimensional simulation is executed by implementing the MHD Lagrangian-remap code (Lare3d) of Arber et al. (2001). The numerical code solves the resistive MHD equations for the fully ionised plasma with a heat flux included in the energy equation (Botha et al., 2011, 2012). Thermal conduction is considered to be included along the magnetic field lines in the form of a classical Spitzer-Härm (1953) or Braginskii conductivity with $\log \Lambda = 18.4$ that corresponds to the standard thermal conductivity parallel to the magnetic field of $\kappa_{\parallel} = 10^{-11} T^{5/2} \text{ W m}^{-1} \text{ K}^{-1}$ (Priest, 2000; Botha et al., 2012). The numerical code consists of an artificial resistivity that is activated only when the **electric** current exceeds a critical value, which is set in the present case **to** $j_c = 2 \text{ mA}$ (Botha et al., 2012). This resistivity is considered in the form given as follows

$$\eta = \begin{cases} \eta_0, & |j| \geq j_c, \\ 0, & |j| < j_c, \end{cases} \quad (1)$$

where η_0 is the anomalous resistivity. η_0 is switched on when the kink instability occurs and thereafter it remains active for the duration of the simulation (Botha et al., 2011, 2012). The coronal loop is initialised as a straight twisted cylinder in a uniform background temperature and density (Fig. 1) as previously performed by Botha et al. (2012).

The initial conditions of the numerical simulation of the coronal loop is taken from observations of a highly twisted loop (Srivastava et al., 2010). Using the multi-wavelength observations of SOHO/MDI, SOT-Hinode/blue-continuum (4504 Å), G band (4305 Å), Ca II H (3968 Å), and TRACE 171 Å, they observed a highly twisted magnetic loop in AR 10960 during the period 04:43 UT–04:52 UT on 2007 June 4. SOT-Hinode/blue-continuum (4504 Å) observations show that the penumbral filaments of a positive polarity sunspot have counterclockwise twist that may be caused by the clockwise rotation of the spot umbrae and can activate a right-handed helical twist in the loop system. This loop whose one footpoint is anchored in this sunspot, shows strong right-handed twist in chromospheric SOT-Hinode/Ca II H (3968 Å) and coronal TRACE 171 Å images, which was consistent with the Hemisphere Helicity Rule (HHR). The length and the radius of the loop are estimated as $L \approx 80 \text{ Mm}$ and $a \approx 4.0 \text{ Mm}$, respectively. The distance between neighbouring turns of magnetic field lines is estimated as $\approx 10 \text{ Mm}$, which further gives the total twist angle $\Phi = 11.5\pi$ as estimated for a homogeneous distribution of the twist along the loop. This observed twist is much larger than the Kruskal-Shafranov instability criterion ($\Phi > 2\pi$) for the kink instability and later triggers a B5.0 class solar flare that occurred between 04:40 UT and 04:51 UT in this active region. The details of these observational finding are given in Srivastava et al. (2010).

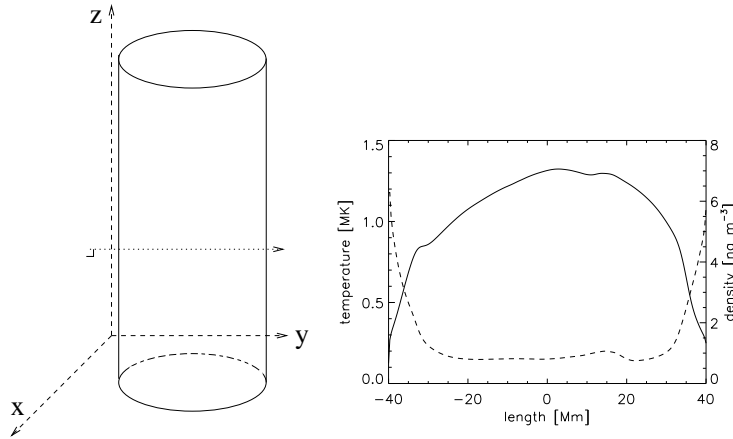


Figure 1: Left-panel: The cartoon shows an orientation of the cylindrical loop in the Cartesian numerical domain. The dotted line indicates about the integration path of the line of sight integral as described by Eq.3 along the y -direction and perpendicular to the $x - z$ plane. Right-panel: Temperature and mass density profiles along the length of the cylindrical loop on its central axis at a time of 579.98 s. The solid (dashed) line is the temperature (density). Initialisation is occurred with a constant temperature of 0.125 MK and a constant density of 1.67 ng m^{-3} .

The observed curved loop is straightened to perform numerical simulations (Figure 1, left-panel). One of the footpoints of the active region loop is anchored in a positive polarity spot (Srivastava et al., 2010) and it is estimated that the minimum value of the magnetic field at this location is 470 G (Botha et al., 2012). From this photospheric value of the magnetic field, the chromospheric field is calculated approximately as 80 G, as well as near the loop apex in the corona as 20 G (Petrie & Patrikeeva, 2009; Botha et al., 2012). The numerical simulation is initialised for the loop with a maximum internal field of 20 G, while the outside background magnetic field is considered as a uniform value of 15 G parallel to the cylindrical axis of the simulated loop structure. In the numerical simulations the coronal loop is initialised as a uniform cylinder in force-free equilibrium and set unstable to an ideal MHD kink instability (Hood et al., 2009; Botha et al., 2012). The axial twist is given by the following equation

$$\Phi = \frac{LB_\theta}{rB_z} \quad \text{with} \quad \max(\Phi) = 11.5\pi, \quad (2)$$

where L is the loop length and r is the radial distance from the central axis of the loop. The axial and azimuthal magnetic fields are given respectively by B_z and B_θ as a function of r . The maximum twist is considered at position $r = 1 \text{ Mm}$, which exceeds the stability threshold, therefore, the loop becomes kink unstable (Mikić et al., 1990). The details of the magnetic field configuration is outlined in Botha et al. (2011, 2012). Gravity is not included in the simulations. The initial temperature and mass density are taken as uniform and constant, with a typical

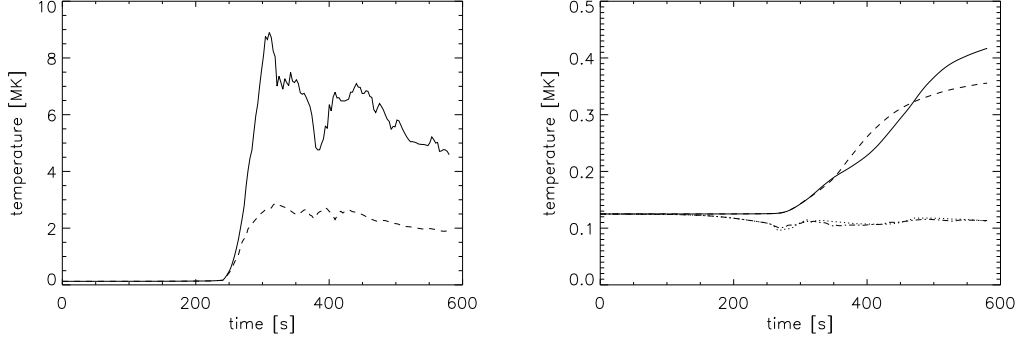


Figure 2: Left-Panel: Maximum temperature during the evolution of the kink instability in which the solid (broken) line is without (with) thermal conductivity. Right-Panel : The average temperature during the evolution of the kink instability in which the solid (broken) line is without (with) thermal conductivity. The minimum temperature is also represented by the dash-dot-dashed (dotted) line without (with) thermal conduction.

values of $1.67 \times 10^{-12} \text{ kg m}^{-3}$ (Young et al., 2009) and 0.125 MK respectively. This temperature is selected to make the evolution of the kink instability as evident in the SDO/AIA filters. During the evolution of the kink instability the temperature increases locally where reconnection occurs in the simulated loop (Botha et al., 2011). This temperature increment is sufficient that the results are highly insensitive to the lower initial temperatures. The initial temperature was chosen specifically so that these high temperatures (Figs. 1, right-panel and 2) will be visible using the SDO/AIA filter response functions (Fig. 3). The details of these technical aspects of the numerical simulation are described in Botha et al. (2012).

3. Synthesized Kink Unstable Loop as an Observable in Various Filters of SDO/AIA

The evolution of the kink unstable coronal loop is studied in the Cartesian geometry (Fig. 1) of the simulation domain. The boundaries in the $x - y$ plane perpendicular to the loop axis are considered at $\pm 8 \text{ Mm}$ and it is set to be reflective. Therefore, there are 4 Mm separation between the loop edge and the outer boundaries to avoid the numerical reflections near the boundaries. Along the loop axis, these boundaries are considered at $\pm 40 \text{ Mm}$ with velocities and temperature fixed respectively at zero and the initial background value by allowing the temperature gradients. Therefore, the heat flux across the ends of the loops exists in the simulation domain. The grid resolution in $x - y - z$ is given by $128 \times 128 \times 256$. These technical details are summarized in Botha et al. (2012).

The images generated from the numerical simulations were obtained by using the modified temperature response functions of SDO/AIA (Aschwanden & Boerner,

2011). Details of the line contributions for the AIA channels are outlined in O'Dwyer et al. (2010) also. The emission is calculated at every node of the numerical grid and thereafter integrated along the y -direction perpendicular to the axis of the simulated loop (cf., Fig. 1, left-panel). The line of sight intensity integral is given by

$$I = \int_{-L_y}^{+L_y} g(T) \rho^2 dy \quad (3)$$

where I , $g(T)$, ρ are respectively the measured intensity, the temperature response function of the various AIA filters, and the mass density. Fig. 3 presents the temperature response functions of all AIA filters. This integration produces intensity images in the $x - z$ plane, which are then integrated over time with the typical time interval determined by the exposure time for SDO/AIA as 2.9 s. After this procedure, the time integrated image is degraded by spatially averaging over squares of $0.375 \times 0.375 \text{ Mm}^2$ to compensate for the pixel resolution of SDO/AIA. The similar process is adopted for the generation of synthesised TRACE observables as reported by Botha et al. (2012). However, in the present study, we perform this image synthesis of the kink unstable loop as an observable in various filters of SDO/AIA (cf., Figs. 4-6). **It should be noted that we used corrected AIA 94 response function with correction for enhanced response at $\log(T) < 6.2$ due to missing Fe IX, Fe XII lines in CHIANTI. Similarly, the response function for AIA 131 Å is used with considering the contribution of Fe VIII and Fe XI. This may vary overall intensity features in the synthesized images of 94 Å and 131 Å compared to those generated by using old response functions. The 94 Å, 211 Å and 131 Å images are synthesized by choosing the elimination of lowest 1% of the intensity values at time 321.9 s.**

After initialisation, the simulated kink unstable loop evolves through a linear phase with a duration of 300 s (Fig. 2). During the nonlinear phase, the kink instability drives magnetic field into a current sheet where reconnection occurs and the temperature reaches to a maximum value due to the released energy and subsequent heating. Thereafter, thermal conduction along the magnetic field lines transports the generated heat flux along the field lines away from the reconnection sites where the plasma was heated. The time-scale for the evolution of the kink instability in all SDO/AIA filters is the same as of the case without thermal conduction. The physical processes during the kink instability, with and without thermal conduction, are discussed in comprehensive manner by Botha et al. (2011) and Botha et al. (2012). In the present numerical simulations, the thermal conductivity causes the spread of temperature along the magnetic field lines resulting in the synthesized images in which the features are less resolved.

The synthesized images show that the footpoints of the loops increase their emission during the nonlinear phase of the kink instability irrespective of the inclusion or exclusion of thermal conductivity. The line of sight intensity integral (Eq.3) is determined by the temperature response function of SDO/AIA and the chosen mass density. Fig. 1 (right-panel) gives the temperature and mass

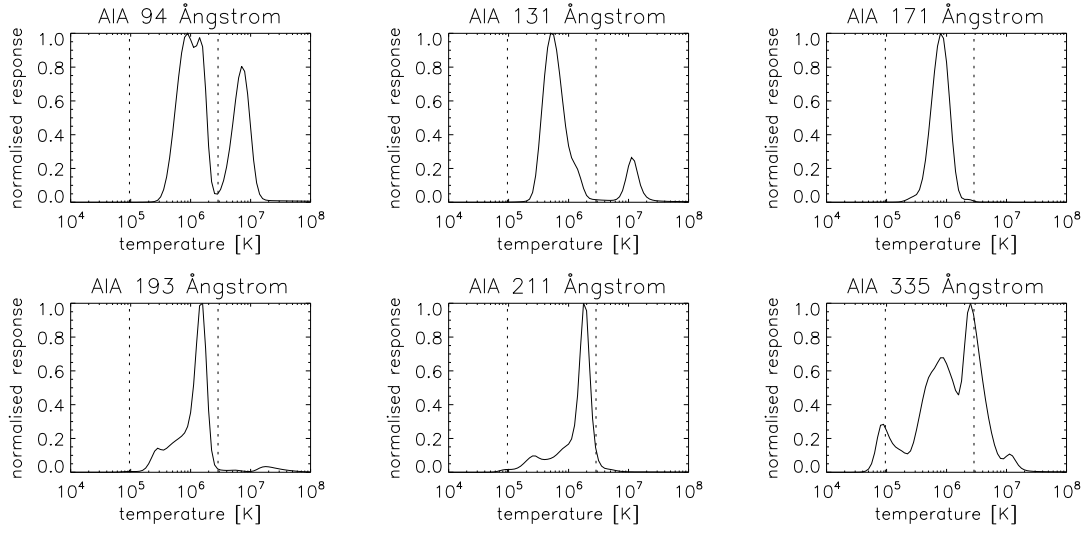


Figure 3: Normalised SDO/AIA temperature response functions with the minimum and maximum temperatures during the simulation represented by vertical dotted lines. The 304 Å band captures chromospheric and transition region temperatures, features that are not included in our model. Consequently it is not included with the other filters.

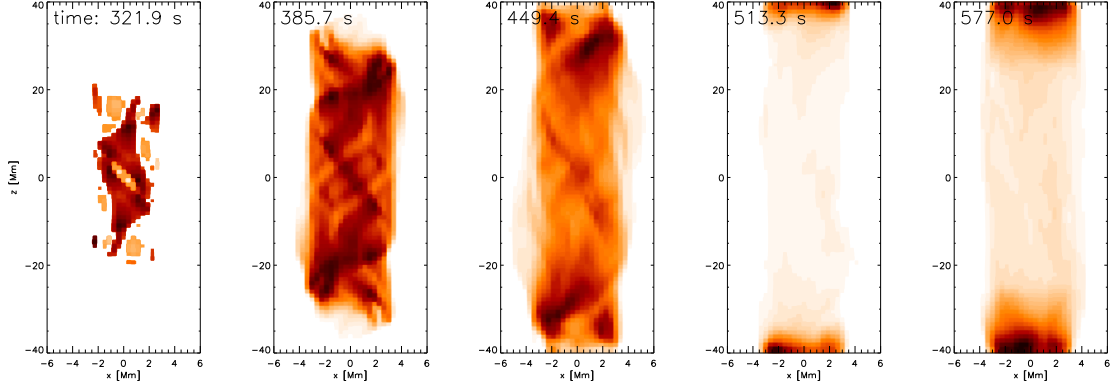


Figure 4: AIA 94 Å **simulations** with exposure time 2.9 s and spatial resolution 0.375 Mm per pixel. The intensity is in reverse colour, with white the lowest value on the scale. This minimum is chosen so that the lowest 1% of the values at time 321.9 s are eliminated from these plots. All the exposures use the same reverse colour scale.

density profiles for the numerical simulation including thermal conduction. It is noticeable that the enhanced emission is due to a density increase at the footpoints of the simulated loop and it is not due to the footpoint heating. Plasma flows from the middle of the numerical domain where the current sheets are formed as reconnection sites, driven by MHD ponderomotive forces generated during the evolution of the kink instability. Footpoint brightening due to compression were also evident in the coronal loop simulations of Haynes & Arber (2007) and Botha et al. (2012). The factor that determines the initiation of the nonlinear phase of the kink instability is the initial twist (Eq.2) in the coronal loop. A smaller value of maximum twist increases the duration of the linear phase and vice versa. However, it is found that once the nonlinear phase is evolved, the formation of the current sheet, the reconnection, and the thermal aftermath have the same duration as long as the initial twist exceeds the stability threshold (Botha et al., 2012). These physical and technical details are discussed in detail by Botha et al. (2012).

During the study of the evolution of such kink instability and its comparison with the observations, it is more realistic to compare the obtained results when thermal conduction is included in the numerical simulation model. The first snapshot in Fig. 4 is synthesized at 321.9 s for AIA 94 Å and shows the twisted structure of the current sheet formed at the initiation of the nonlinear phase of the evolution of kink instability. In the later images, the thermal conduction has transported the reconnection generated heat flux from the internal reconnection sites along the magnetic field lines. As the internal reconnection occurs within the simulated loop, the magnetic field lines become straight along the length of the loop (Haynes & Arber, 2007; Botha et al., 2012). At the same time, the heat flux is transported along magnetic field lines away from the reconnection sites. Therefore, the loop becomes cool and its internal magneto-plasma structures

are less resolved (Botha et al., 2012).

The corrected and modified temperature response functions for the various wavebands (filters) of SDO/AIA are presented in Fig. 3. The emissions in 171 Å for SDO/AIA and TRACE are almost the same. The only difference between these two observational instruments is the time resolution. The TRACE exposure time is approximately eleven times longer than that of the SDO/AIA. Therefore, the images from SDO/AIA are much sharper. Botha et al. (2012) have already reported the kink unstable loop as an observable in TRACE 171 Å filter, therefore, we do not present the similar results as obtained in AIA 171 Å filter. In the present paper, we report the evolution of observed kink unstable loop as an observable in the high-temperature filters of SDO/AIA. Moreover, AIA 193 Å and 211 Å filter responses are almost similar, therefore, we present only the results related to the 211 Å synthesized AIA images. The 304 Å band captures chromospheric and transition region temperatures and related features that are not included in our model.

The emission images for SDO/AIA 94 Å, 131 Å and 211 Å are presented in Figs. 4-6. As each temperature response function (Fig. 3) is different from the others, the structures visible by each waveband are slightly different. The temperature response function for SDO/AIA 94 Å captures the top half of the temperatures obtained during the simulation, so that the heated magnetic structures inside the loop are visible in the intensity images, together with the average temperature inside the loop (Fig. 4). The temperature response function of SDO/AIA 131 Å captures the middle of the temperature range during the simulation, so that the intensity images (Fig. 5) shows mainly loop structure at the average temperature. The images obtained for SDO/AIA 211 Å (Fig. 6) captures the maximum temperature during the simulation, with a contribution from the average and lower temperatures, as shown by its temperature response function (Fig. 3). The emission images of SDO/AIA 304 Å (Fig. 3) are not presented in this study. This waveband captures the temperatures of the chromosphere and transition region, which are not included in our coronal loop model. Also, the emission images obtained for SDO/AIA 335 Å are not presented here. This temperature response function is broad and spans all the temperatures generated in the simulation. As a result, 70% or more of the lower values of the intensity obtained by (Eq.3) have to be eliminated in order to produce intensity plots in which the loop structure is clearly visible.

4. Discussions and Conclusion

A highly twisted and kink unstable coronal loop is studied numerically by solving the resistive MHD equations for a fully ionised plasma and with the inclusion of the thermal conduction. The loop is initialised as a straight cylinder with a very high twist above the stability threshold leading to the kink instability. The simulations were initialised with physical parameters derived from the observations of a highly twisted coronal loop (Srivastava et al., 2010). The initial magnetic field structure used in the simulations is considered as a kink-unstable force-free equilibrium where the twist varies with radius (Hood et al.,

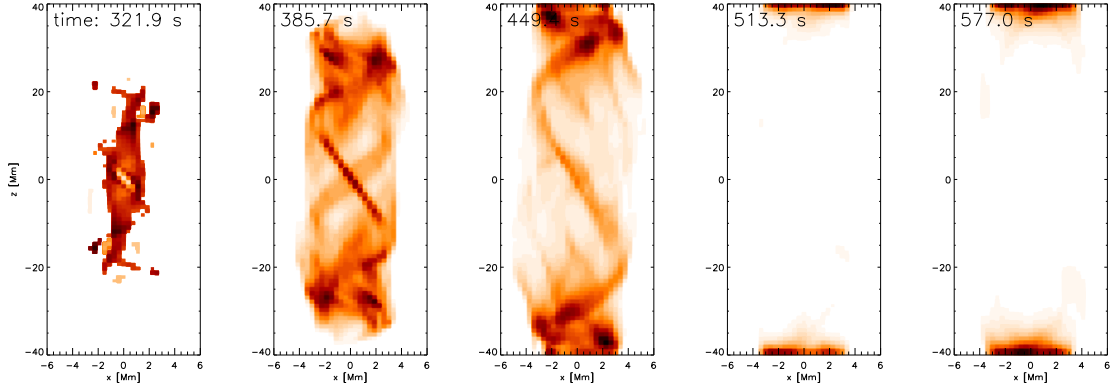


Figure 5: AIA 131 Å simulations with exposure time 2.9 s and spatial resolution 0.375 Mm per pixel. The intensity is in reverse colour, with white the lowest value on the scale. This minimum is chosen so that the lowest 1% of the values at time 321.9 s are eliminated from these plots. All the exposures use the same reverse colour scale.

2009; Botha et al., 2012). Line of sight emission intensities were calculated from the simulation data using the corrected temperature response functions from SDO/AIA. The different wavebands from the SDO/AIA exhibits different magnetic field structures, as each filter temperature response function captures a different plasma temperature and related emissions. Therefore, it becomes plausible to study many high-resolution features of a highly twisted kink-unstable coronal loop as observables of the various filters of SDO/AIA. During the evolution of the kink instability, the internal structure of the synthesized loop is shown in the generated images (Figs. 4-6). This structure is transformed into a simpler magnetic configuration as the kink instability triggers multiple reconnections that cause the straightening of the internal magnetic field. The kink instability heats the plasma near the current sheet due to the reconnection. This heat flux is transported along the magnetic field lines away from the reconnection sites due to thermal conduction. Therefore, the temperature maximum in the simulation is lower compared to the case when thermal conduction is excluded from the model (Botha et al., 2012).

The observations by Srivastava et al. (2010) clearly shows that after the heating as well as activation of high twist, the loop plasma is condensed down within few minutes and becomes invisible in coronal filters. The duration of the simulations exhibits 4.25 minutes of the nonlinear evolutionary phase of the kink instability. During this time span the average temperature of the loop increases (Fig. 2, right-panel) while the maximum temperature with the thermal conduction is almost unchanged (Fig. 2, left-panel). The reason may be that the current sheets evolve through the multiple reconnection process instead of continuous heating episode. Therefore, the heating location moves in the simulated loop (Hood et al., 2009). Footpoint brightening due to compression of the plasma is also evident in the simulation, however, it is not evident from

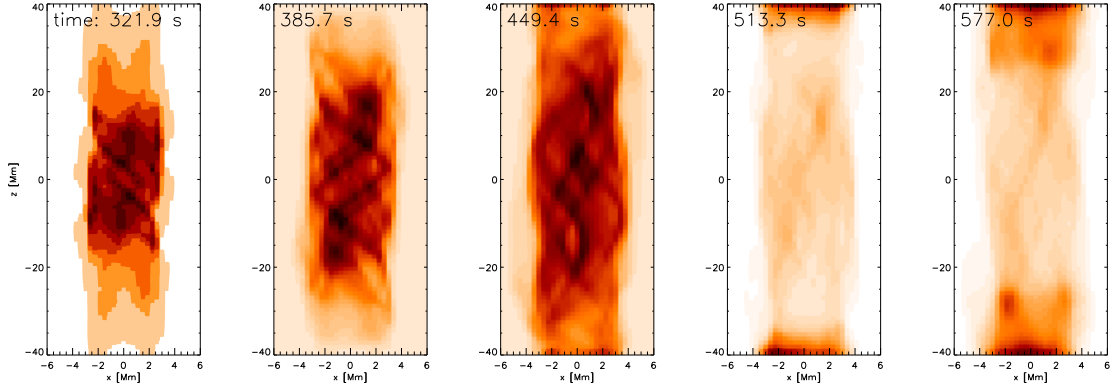


Figure 6: AIA 211 Å with parameters and times as in Figure 4. The minimum (white) of the intensity scale is chosen so that the lowest 1% of the values at time 321.9 s are eliminated from these plots. All the exposures use the same reverse colour scale.

the coronal observations by Srivastava et al. (2010). Although, Srivastava et al. (2010) have observed brightpoints at chromospheric temperatures that may be the evidence of localized footpoint heating in lower atmosphere.

In conclusion, we extend the works of Botha et al. (2012) and show that how the kink unstable observed loop will be synthesized in various high-temperature filters of SDO/AIA. The physical scenario and the technical details of the numerical simulation presented in the paper are very similar to the Botha et al. (2012). However, the present work demonstrates about the synthesis of the observational signature of coronal kink instability in the various filters of SDO/AIA and discuss its physical significance. More studies should be performed using forthcoming observations from SDO/AIA regarding the helical kink unstable loops that may shed more light on the stringent simulation initial conditions, and can provide more understanding of the energy generation and transport in the coronal loop systems during the evolution of such instability.

Acknowledgments We thank both the reviewers for their suggestions that improved the manuscript. The use of LARE3d code is acknowledged in the present work. **This work was partly funded by the UK Science and Technology Facilities Council under grant number ST/I000720/1.** AKS acknowledges the financial support from DST-RFBR-P117 project, and also acknowledges Shobhna Srivastava for patient encouragements.

References

- Arber, T. D., Longbottom, A. W., & Van der Linden, R. A. M. 1999, *Astrophys. J.*, 517, 990
- Arber, T. D., Longbottom, A. W., Gerrard, C. L., & Milne, A. M. 2001, *J. Comput. Phys.*, 171, 151

- Aschwanden, M. J., & Boerner, P., 2011, *Astrophys. J.* , 732, 81
- Botha, G. J. J., Arber, T. D., & Hood, A. W. 2011, *Astron. Astrophys.* , 525, A96
- Botha, G. J. J., Arber, T. D., & Srivastava, A. K. 2012, *Astrophys. J.* , 745, 53
- Baty, H., & Heyvaerts, J. 1996, *Astron. Astrophys.* , 308, 935
- Browning, P. K., Gerrard, C., Hood, A. W., Kevis, R., & Van der Linden, R. A. M. 2008, *Astron. Astrophys.* , 485, 837
- Cho, K.-S., Lee, J., Bong, S.-C., et al. 2009, *Astrophys. J.* , 703, 1
- Foullon, C., Verwichte, E., Nakariakov, V. M., Nykyri, K., & Farrugia, C. J. 2011, *Astrophys. J. Lett.* , 729, L8
- Gerrard, C. L., Arber, T. D., & Hood, A. W. 2002, *Astron. Astrophys.* , 387, 687
- Haynes, M., & Arber, T. D. 2007, *Astron. Astrophys.* , 467, 327
- Haynes, M., Arber, T. D., & Verwichte, E. 2008, *Astron. Astrophys.* , 479, 235
- Hood, A. W., & Priest, E. R. 1979, *Solar Phys.* , 64, 303
- Hood, A. W., Browning, P. K., & Van der Linden, R. A. M. 2009, *Astron. Astrophys.* , 506, 913
- Innes, D. E., Cameron, R. H., Fletcher, L., Inhester, B., & Solanki, S. K. 2012, *Astron. Astrophys.* , 540, L10
- Kliem, B., Török, T. 2006, *Physical Review Letters*, 96, 255002
- Kozlova, L. M., & Somov, B. V. 2009, *Moscow University Physics Bulletin*, 64, 541
- Kumar, P., Srivastava, A. K., Somov, B. V., et al. 2010, *Astrophys. J.* , 723, 1651
- Liu, R., Alexander, D., & Gilbert, H. R. 2007, *Astrophys. J.* , 661, 1260
- Liu, R., Gilbert, H. R., Alexander, D., & Su, Y. 2008, *Astrophys. J.* , 680, 1508
- Mikić, Z., Schnack, D. D., & Van Hoven, G. 1990, *Astrophys. J.* , 361, 690
- Moser, A. L., & Bellan, P. M. 2012, *Nature* , 482, 379
- O'Dwyer, B., Del Zanna, G., Mason, H. E., Weber, M. A., & D. Tripathi, D. 2010, *Astron. Astrophys.* , 521, A21
- Petrie, G. J. D., & Patrikeeva, I. 2009, *Astrophys. J.* , 699, 871

- Priest, E. R. 2000, Solar Magnetohydrodynamics, Geophysics and Astrophysics Monographs, Volume 21, (Dordrecht: D. Reidel Publishing Company), Section 2.3.2
- Spitzer, L., & Härm, R. 1953, Physical Review, 89, 977
- Srivastava, A. K., Zaqarashvili, T. V., Kumar, P., & Khodachenko, M. L. 2010, *Astrophys. J.* , 715, 292
- Young, P. R., Watanabe, T., Hara, H., & Mariska, J. T. 2009, *Astron. Astrophys.* , 495, 587
- Zaqarashvili, T. V., Díaz, A. J., Oliver, R., & Ballester, J. L. 2010, *Astron. Astrophys.* , 516, A84